

Quasi-periodicity in the wake of a rotationally oscillating cylinder

By SEUNG-JIN BAEK AND HYUNG JIN SUNG†

Department of Mechanical Engineering, Korea Advanced Institute of Science and Technology,
373-1, Kusong-dong, Yusong-ku, Taejeon, 305-701, Korea

(Received 30 March 1999 and in revised form 1 December 1999)

A systematic numerical analysis is performed for the quasi-periodicity in the wake where a circular cylinder is rotationally oscillated in time. The main emphasis is placed on the identification of frequency selection subjected to the controlled perturbations in the vicinity of lock-on. The frequency responses are scrutinized by measuring the lift coefficient (C_L). A direct numerical simulation is made to portray the unsteady dynamics of wake flows at $Re = 110$. It is found that, after the shedding frequency is bifurcated at the boundary of lock-on, one frequency follows the forcing frequency and the other gradually converges to the natural shedding frequency. The asymptotic convergence phenomena are observed by solving the Van der Pol equation and the circle map. A new frequency selection formula is proposed. The quasi-periodic states are interpreted in terms of the forcing frequency, shedding frequency and modulated frequencies by employing the torus concept and the $C_L(t)$ diagram. In the quasi-periodic state, the variation of magnitudes and relevant phase changes of C_L with forcing phase are examined.

1. Introduction

Much work has been reported on the shedding of vortices from a circular cylinder which is placed in an oncoming crossflow (Sarpkaya 1979; Bearman 1984; Oertel 1990; Griffin & Hall 1991; Williamson 1996). The so-called Kármán vortices are shed to the rear of the cylinder and they persist for some distance downstream in the wakes. Many investigations have also been made of the near-wake flow structure subjected to controlled forcings. These studies were performed to understand the interrelation between the near-wake flow structure and the forcing on the body. In general, relatively simple forcing methods on the cylinder have been employed, e.g. in-line vibration, cross-stream vibration (Bishop & Hassan 1964; Koopman 1967; Stansby 1976; Ongoren & Rockwell 1988; Chyu & Rockwell 1996) and rotational oscillation (Tokumaru & Dimotakis 1991). One prominent issue is the lock-on phenomenon of the shedding frequency on the imposed frequency, i.e. the shedding frequency synchronizes with the forcing frequency (Sung, Hwang & Hyun 1994*a*; Sung, Kim & Hyun 1994*b*).

A literature survey reveals that most of the studies of near-wake flow structure subjected to controlled perturbations have been concerned with the excitation of the cylinder at a frequency in the vicinity of the inherent vortex formation frequency. The ‘lock-on’ excitation produces a resonant peak of the amplitude of the flow state quantity (Koopman 1967; Stansby 1976; Griffin & Hall 1991; Filler, Marston & Mih

† Author to whom correspondence should be addressed: e-mail hjsung@kaist.ac.kr.

1991; Baek & Sung 1998). However, the outer boundaries of the region of 'lock-on' are characterized by the onset of quasi-periodic and chaotic states. Van Atta & Gharib (1987) demonstrated the generation of a multiplicity of spectral components experimentally. Very small cylinder vibrations produced a coupled wake-cylinder response. The velocity spectra associated with these coupled motions had dominant peaks at sum and difference combinations of multiples of the Strouhal frequency and the forcing frequency. In the window of chaos, the velocity spectra were broadened by switching between different competing coupling modes. Karniadakis & Triantafyllou (1989) numerically simulated the response of the near wake and defined the regions of quasi-periodic and chaotic behaviour. These wake responses were interpreted in terms of multiple peaks of spectra and aperiodic phase-plane trajectories. Blevins (1985) explored the influence of sound on vortex shedding. He found that the frequency of vortex shedding can be shifted by sound applied either above or below the nominal vortex shedding frequency. Lofty & Rockwell (1993) asserted in their experiment that the response of the near wake can be classified into two general categories: a modulated wake and a phase-locked wake. They analysed the wakes by using the crucial topological features of the near wake and a phase clock concept.

As mentioned above, although only one frequency component is forced, the cylinder wake generates multiple frequency components after a bifurcation of frequency. This state can be called the 'quasi-periodicity', where the state has a period of infinity and does not close itself in the phase-plane. The Fourier transform of the periodic state consists of delta function spikes located at integer multiples of the fundamental frequency. The quasi-periodicity state can be thought of as a mixture of periodic motions of several different fundamental frequencies. The Fourier transform of the quasi-periodic system consists of delta function spikes at all integer combinations of fundamental frequencies. Since it contains only discrete components, it should be distinguished from a chaotic system that has a broad continuous component distribution (Ott 1993).

Based on the preceding observations of quasi-periodicity, this study presents a systematic numerical analysis of the near-wake frequency selection and the asymptotic states. The main emphasis of the present study is to identify the quasi-periodic state around the lock-on region. Among the excitations in the vicinity of the outer boundary of the lock-on region, a new frequency selection mechanism is observed in a modulated wake. At the boundary between lock-on and non-lock-on, the shedding frequency is bifurcated. After the bifurcation, one frequency follows the forcing frequency (S_f) and the other returns to the natural shedding frequency (St_0^*). Unlike most previous investigations, the shedding frequency (St_0) approximates the natural shedding frequency. This is an asymptotic convergence of the shedding frequency to the natural shedding frequency. These converging phenomena of St_0 to St_0^* are ascertained by solving the Van der Pol equation and the circle map (Nayfeh & Mook 1979; Strogatz 1994). The power spectral density plots are used to analyse the frequency response. A new frequency selection formula is proposed which depends on the natural shedding and the forcing frequencies. It is found that this formula provides a satisfactory fit to the present numerical simulation results.

A direct numerical simulation is made in the present study to portray the unsteady dynamics of wake flows behind a circular cylinder. The Reynolds number based on the diameter (D) is fixed at $Re = 110$, at which the vortex shedding flow is assumed to be two-dimensional (Williamson 1996). Excitation is given by the rotational oscillation of a circular cylinder (Baek & Sung 1998). The natural shedding frequency is $St_0^* = 0.171$ and the forcing frequency (f^o) varies in the range $0.150 \leq S_f = f^o D / U_\infty \leq 0.190$. The

maximum rotation velocity (Ω_{max}) is 5.0% of the free-stream velocity. The primary advantage of the numerical simulation is that wide ranges of the relevant flow variables can be encompassed.

2. Numerical method

The non-dimensional governing equations for an unsteady incompressible flow are

$$\frac{\partial u_i}{\partial t} + \frac{\partial}{\partial x_j} u_i u_j = -\frac{\partial p}{\partial x_i} + \frac{1}{Re} \frac{\partial}{\partial x_j} \frac{\partial}{\partial x_j} u_i, \quad (2.1)$$

$$\frac{\partial u_i}{\partial x_i} = 0, \quad (2.2)$$

where x_i are the Cartesian coordinates and u_i velocity components in each direction. The free-stream velocity U_∞ and the cylinder diameter D are used for non-dimensionalization. The Reynolds number is defined as $Re = U_\infty D / \nu$, where ν is the kinematic viscosity.

To simulate wake flows behind a cylinder, it is useful to transform the governing equations (2.1) and (2.2) into the generalized coordinates y^i (Choi, Moin & Kim 1992). The velocity components u_i are transformed into the volume fluxes across the faces of the cell q^i . Formulation of the problem in terms of the contravariant velocity components, weighted with the Jacobian J in conjunction with the staggered variable configuration, leads to discretized equations. The resulting pressure Poisson equation is solved, where the discretized mass conservation is satisfied. The transformed governing equations are rewritten as

$$\frac{\partial q^i}{\partial t} + N^i(q) = -G^i(p) + L_1^i(q) + L_2^i(q), \quad (2.3)$$

$$D^i q^i = \frac{1}{J} \left(\frac{\partial q^1}{\partial y^1} + \frac{\partial q^2}{\partial y^2} \right) = 0, \quad (2.4)$$

where N^i is the convection term, $G^i(p)$ is the pressure gradient term, L_1^i and L_2^i are the diffusion terms without and with cross-derivatives and D^i is the divergence operator, respectively. The terms in equation (2.3) are rewritten in the following form:

$$N^i(q) = \frac{1}{J} \gamma_m^i \frac{\partial}{\partial y^j} \frac{1}{J} c_k^m q^k q^j, \quad (2.5)$$

$$G^i(p) = \alpha^{ij} \frac{\partial p}{\partial y^j}, \quad (2.6)$$

$$L_1^i(q) = \frac{1}{Re} \frac{1}{J} \gamma_m^i \frac{\partial}{\partial y^k} \alpha^{kj} \frac{\partial}{\partial y^j} \frac{1}{J} c_l^m q^l, \quad j = k, \quad (2.7)$$

$$L_2^i(q) = \frac{1}{Re} \frac{1}{J} \gamma_m^i \frac{\partial}{\partial y^k} \alpha^{kj} \frac{\partial}{\partial y^j} \frac{1}{J} c_l^m q^l, \quad j \neq k, \quad (2.8)$$

where

$$q^j = \gamma_k^j u_k, \quad c_k^j = \partial x_j / \partial y^k, \quad \gamma_k^j = J(c_k^j)^{-1},$$

$$\alpha^{jk} = J(c_j^m c_k^m)^{-1}, \quad J = (\|c_j^m c_k^m\|)^{1/2}, \quad j, k, l, m = 1, 2.$$

A fully implicit, fractional-step method composed of four-step time advancement

is used to solve the governing equations (Choi, Moin & Kim 1993). The fractional step, or time-split method, is in general a method of approximation of the evolution equations based on decomposition of the operators they contain. In application of this method to the Navier–Stokes equations, one can interpret the role of pressure in the momentum equations as a projection operator which projects an arbitrary vector field into a divergence-free vector. In the Cartesian coordinates, these four steps are

$$\frac{\hat{u}_i - u_i^n}{\Delta t} + \frac{1}{2} \frac{\partial}{\partial x_j} (\hat{u}_i \hat{u}_j + u_i^n u_j^n) = -\frac{\partial p^n}{\partial x_i} + \frac{1}{2} \frac{1}{Re} \frac{\partial}{\partial x_j} \frac{\partial}{\partial x_j} (\hat{u}_i + u_i^n), \quad (2.9)$$

$$\frac{\check{u}_i - \hat{u}_i}{\Delta t} = \frac{\partial p^n}{\partial x_i}, \quad (2.10)$$

$$\frac{\partial}{\partial x_i} \frac{\partial p^{n+1}}{\partial x_i} = \frac{1}{\Delta t} \frac{\partial \check{u}_i}{\partial x_i}, \quad (2.11)$$

$$\frac{u_i^{n+1} - \check{u}_i}{\Delta t} = -\frac{\partial p^{n+1}}{\partial x_i}. \quad (2.12)$$

A second-order central difference scheme is used for the spatial derivatives and a Crank–Nicolson method is employed in the time advancement. The substitution of equations (2.10) and (2.12) into equation (2.9) indicates that the present scheme is second-order accurate in time. The discretized nonlinear momentum equations are solved by using a Newton-iterative method. Solving the Poisson equation for p satisfies the continuity equation. In this computation, equations (2.9)–(2.12) are also transformed from the Cartesian coordinate to the generalized coordinate.

A C-mesh is used for the present simulation. This type of mesh is ideally suited for simulating wake flows since better streamwise resolution can be provided in the wake region. The use of a C-mesh also simplifies the application of outflow boundary conditions. The outflow boundaries are located at $20D$ and the transverse boundaries are at $30D$, which corresponds to $(x, y) = (321 \times 101)$. Uniform free-stream velocity is prescribed at the inflow and far-field boundaries, and a convective boundary condition is employed at the outflow boundary in order to smoothly convert the disturbances out of the computational domain (Pauley, Moin & Reynolds 1990). On the cylinder wall, the periodic rotational oscillation conditions are used.

Since the cylinder is rotated sinusoidally in time t^o at a forcing rotational frequency f^o , the non-dimensional cylinder rotation velocity (Ω) is expressed by

$$\Omega = \Omega_{max} \sin(2\pi S_f t), \quad (2.13)$$

where the quantities are non-dimensionalized by adopting the following relations: $t = t^o U_\infty / D$ and $S_f = f^o D / U_\infty$. Here, the superscript o denotes the dimensional counterpart. The maximum rotation velocity Ω_{max} is 5.0% of the free-stream velocity ($\Omega_{max} = 0.05$) and this magnitude can couple the forcing frequency with the natural shedding frequency. Based on equation (2.13), the counter-clockwise rotation occurs in the period of up to $0.5T$ from $0T$. Then, the clockwise rotation occurs from $0.5T$ to T . Accordingly, the counter-clockwise rotation velocity is maximum at $0.25T$ and the clockwise one is maximum at $0.75T$. Here, T denotes the non-dimensional forcing period, i.e. $U_\infty / f^o D = 1/S_f$. Details regarding the flow configuration, boundary conditions, grid resolution and other numerical procedures are compiled in Baek & Sung (1998).

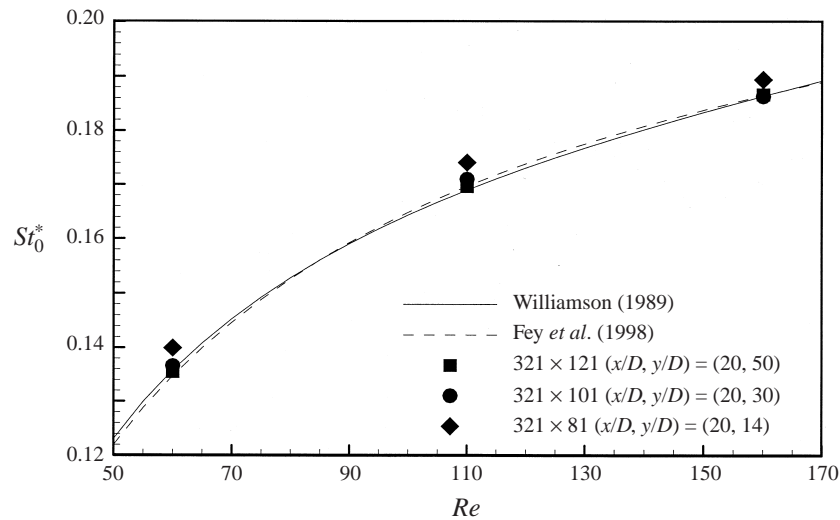


FIGURE 1. The natural frequency (St_0^*) as a function of Reynolds number (Re) for the different transverse boundary sizes.

3. Frequency selection in the wakes

The reliability and accuracy of the present simulation have been ascertained in the previous paper (Baek & Sung 1998). The cylinder wake at $Re = 110$ has a two-dimensional periodic laminar vortex shedding. The $St_0^* - Re$ formulae in the range $50 \leq Re \leq 160$, pertinent to parallel vortex shedding, have been obtained by Williamson (1989) and Fey, König & Eckelmann (1998). Several trial calculations were repeated to monitor the sensitivity of the results to grid size, where the grid points are crowded near the wall boundary. The grid convergence was checked (figure 1) and the outcome of these tests was found to be satisfactory for the present two-dimensional computations $(x, y) = (321 \times 101)$. The value predicted by the present simulation at $Re = 110$ is $St_0^* = 0.171$, which is in good agreement with that obtained from the experimental formulae.

Time histories of the lift coefficient (C_L) taken from the non-dimensional time $t = 1000$ to $t = 1500$ are shown in figure 2. When the oscillation is not imposed, i.e. no forcing, the wake exhibits natural shedding as shown in figure 2(a). The natural shedding frequency is $St_0^* = 0.171$. Next, the frequency responses subjected to the forced oscillations are investigated. An inspection of the time histories of C_L as shown in figure 2(b-j) reveals that lock-on occurs in the cases of (e) $S_f = 0.165$, (f) $S_f = 0.170$ and (g) $S_f = 0.175$. The lock-on range is relatively narrow because the magnitude of forcing is not large ($\Omega_{max} = 0.05$). In these cases, the near-wake vortex pattern is highly repeatable over the cycles.

Outside the relatively narrow band of lock-on, the flow structure is not phase-locked with respect to the forced oscillation. A modulated wake pattern is observed over ranges of excitation frequency above and below the lock-on range. In the cases below the lock-on range ($S_f = 0.150, 0.155$ and 0.160) and above the lock-on range ($S_f = 0.180, 0.185$ and 0.190), additional frequency components exist. The modulated behaviour below the lock-on range is analogous to that occurring at excitations above the phase locking. In general, it is shown that the modulated long period decreases as the forcing frequency moves away from the lock-on boundary frequency.

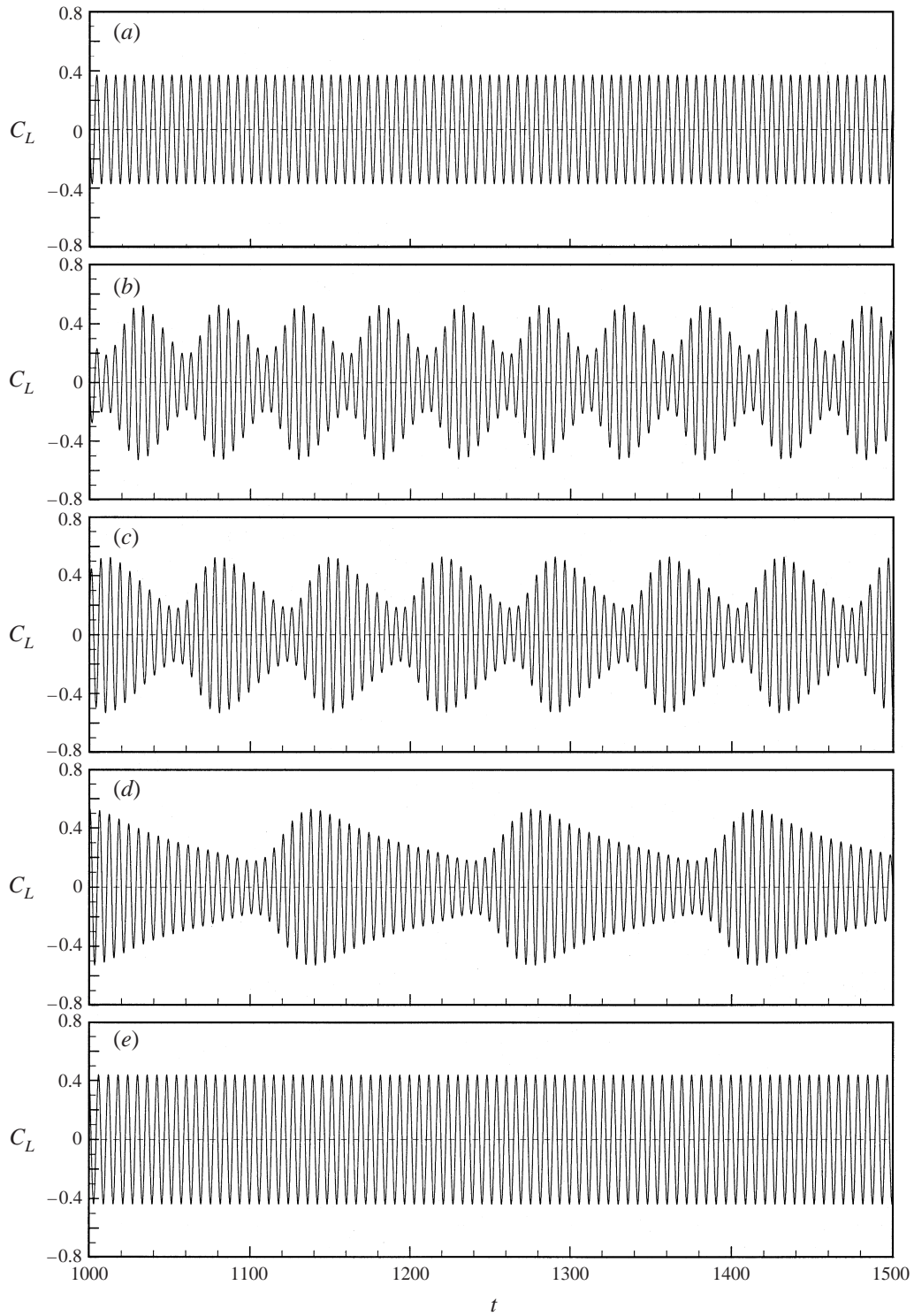


FIGURE 2(a-e). For caption see opposite.

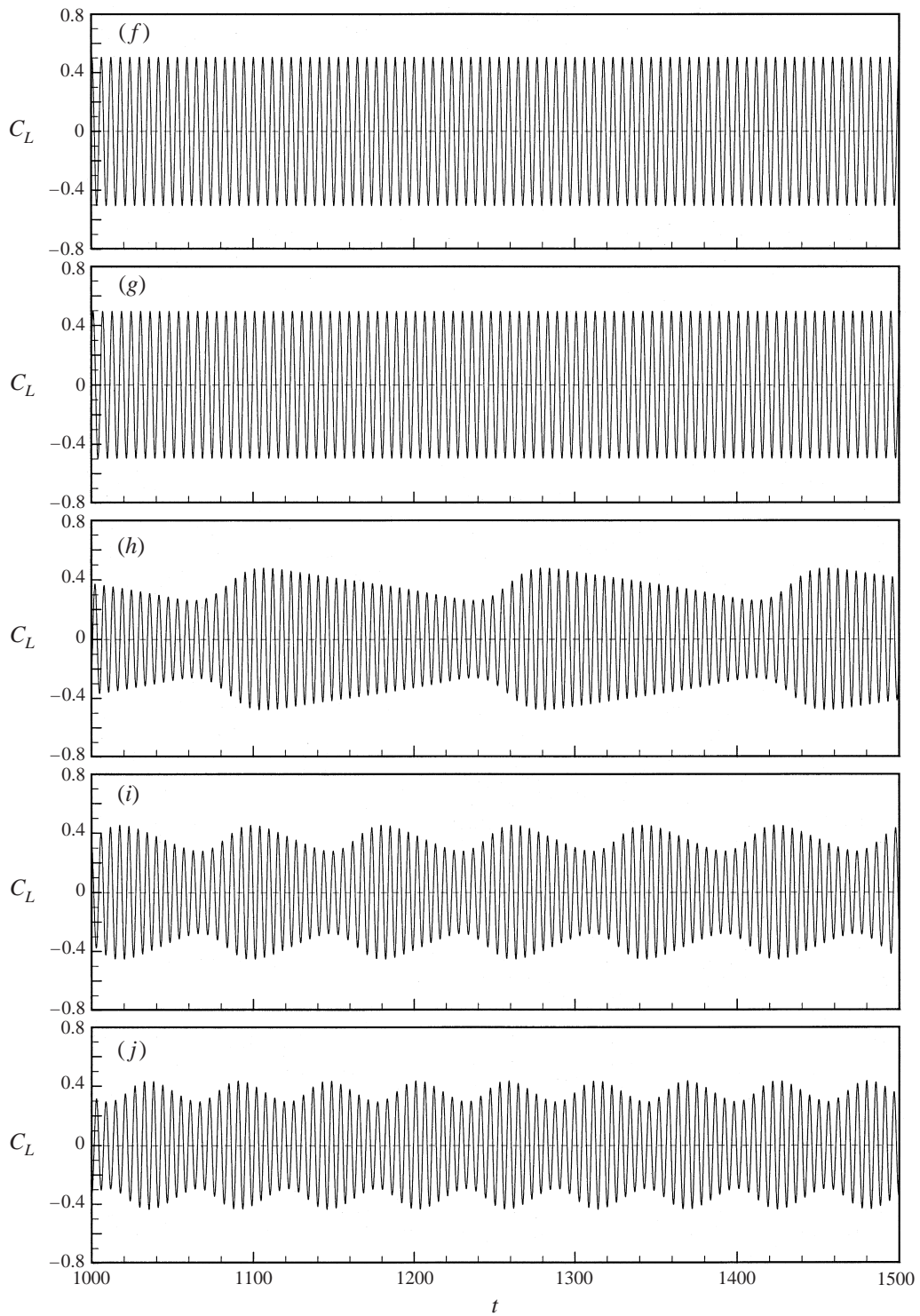


FIGURE 2. Time histories of C_L : (a) no forcing, (b) $S_f = 0.150$, (c) $S_f = 0.155$, (d) $S_f = 0.160$, (e) $S_f = 0.165$, (f) $S_f = 0.170$, (g) $S_f = 0.175$, (h) $S_f = 0.180$, (i) $S_f = 0.185$ and (j) $S_f = 0.190$. $\Omega_{max} = 0.05$.

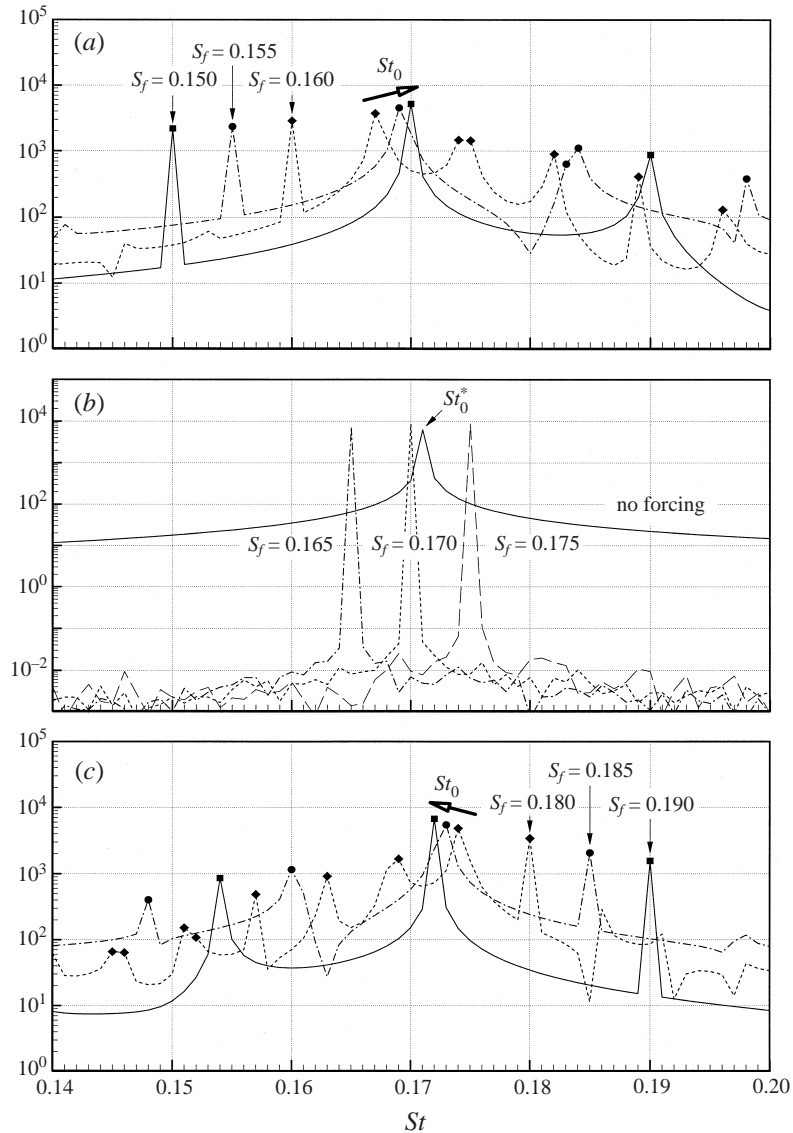


FIGURE 3. Power spectra at several forcings ($\Omega_{max} = 0.05$): (a) below the lock-on region, (b) lock-on region and (c) above the lock-on region.

An examination of the magnitudes of C_L in figure 2 indicates that the peak to peak values of C_L at lock-on are larger than those at no forcing. However, the peak to peak values at non-lock-on vary in time.

In order to analyse the modulated frequency selection in detail, C_L is Fourier transformed and the results are plotted in figure 3. The data from $t = 500$ to 1500 are employed for the transform so that the transform resolution is 0.001. As shown in figure 3(b), when no forcing is imposed, the natural shedding frequency is clearly detected at $St_0^* = 0.171$. In the narrow band of excitation frequencies $S_f = 0.165$, 0.170 and 0.175, the flow is synchronized, which is displayed in figure 3(b). For excitation at frequencies below the lock-on, i.e. $S_f = 0.150$, 0.155 and 0.160, the

frequency selections are exhibited in figure 3(a). A closer inspection of the shedding frequencies (St_0) subjected to several forcing frequencies reveals that they are not concentrated at the natural shedding frequency ($St_0^* = 0.171$), but gradually converge to St_0^* . The forced flow frequency bifurcates into two frequencies: one follows the forcing frequency (S_f) and the other (St_0) asymptotically moves to St_0^* . It is important to find these converging phenomena since they are closely related to the afore-stated quasi-periodicity in the controlled cylinder wakes. For excitation at frequencies above the lock-on, i.e. $S_f = 0.180, 0.185$ and 0.190 , the same behaviour is observed, as exhibited in figure 3(c). Other modulated frequencies due to the nonlinear coupling effect are also detected in figure 3. The additional frequencies follow the rule that the interval between the modulated frequencies is equivalent to the interval between St_0 and S_f .

A magnitude comparison for the respective frequencies shows $St_0 > S_f > S_{m_{j,k}}$, where $S_{m_{j,k}}$ denotes the modulated frequencies. This means that St_0 is dominant compared to S_f and other subsequent modulated frequencies $S_{m_{j,k}}$. The following formula can be derived for generating $S_{m_{j,k}}$ from S_f and St_0 by examining figure 3: $S_{m_{j,k}} = jSt_0 + kS_f$, where j, k are integers. For example, the first modulated frequency $S_{m_{2,-1}}$ is $S_{m_{2,-1}} = 2St_0 - S_f$ for $j = 2, k = -1$ and the second $S_{m_{3,-2}}$ is $S_{m_{3,-2}} = 3St_0 - 2S_f$ for $j = 3, k = -2$, etc. For convenience, the first modulated frequency is abbreviated as $S_{m_{2,-1}} = S_m$ hereafter since it will be referred to frequently in the following sections. It is seen in figure 3 that the modulated frequencies ($S_{m_{j,k}}$) are located on the opposite side of S_f compared to St_0 . The magnitudes of $S_{m_{j,k}}$ decrease as S_f moves away from the lock-on range. On the other hand, as S_f approaches the lock-on boundary, the magnitudes of $S_{m_{j,k}}$ increase and the modulated frequency intervals decrease. When S_f is very close to the lock-on boundary, the interval between S_f and St_0 becomes very narrow and their magnitudes are almost equivalent. This forms a distributed spectral band at the lock-on boundary. As S_f approaches the boundary of lock-on, the responses are characterized by a richness in frequency content and relatively broadened spectral densities. This may be compared with the phenomena of low-order chaos discussed in Karniadakis & Triantafyllou (1989).

It is important to look into the effect of Reynolds number (Re). Two additional simulations have been made for $Re = 80$ and 140 (figure 4). At $Re = 80$, excitation at frequencies below St_0^* has been applied. The case of $S_f = 0.145$ shows the lock-on behaviour. In the quasi-periodic states of $S_f = 0.138$ and $S_f = 0.140$, St_0 increases and converges to St_0^* . At $Re = 140$, excitation at frequencies above St_0^* has been applied. The case of $S_f = 0.188$ shows the lock-on behaviour. In the quasi-periodic states of $S_f = 0.190$ and $S_f = 0.195$, St_0 decreases and converges to St_0^* . The spectral behaviours of $Re = 80$ and 140 are found to be consistent with those of the original Reynolds number $Re = 110$.

The afore-stated frequency bifurcation and the corresponding convergence of St_0 to St_0^* can be observed by solving the Van der Pol equation. The Van der Pol equation is widely used to analyse nonlinear oscillation models, as it exhibits the desired characteristics of limit-cycle oscillation and frequency lock-on. Hartlen & Currie (1970) proposed a Van der Pol-type soft nonlinear oscillator for the lift force, which is coupled to the body motion by a linear dependence on the cylinder velocity. Iwan & Blevins (1974) devised a model in which the vortex-induced oscillation satisfies a Van der Pol-type equation.

The Van der Pol equation of free, self-sustained oscillations is expressed as

$$\ddot{u} + \omega_0^2 u = \epsilon(\dot{u} - 1/3\dot{u}^3) + E(t), \quad (3.1)$$

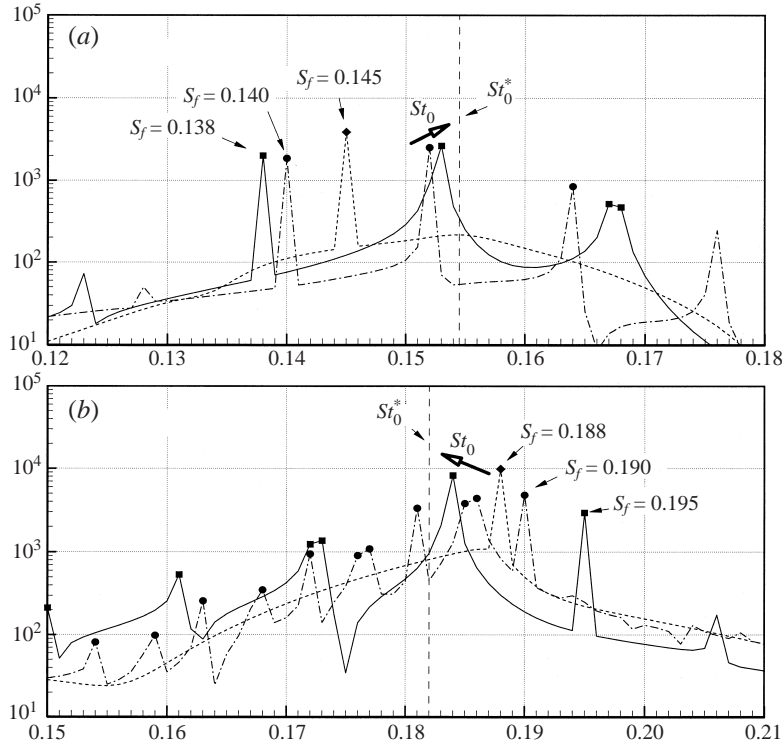


FIGURE 4. Power spectra at (a) $Re = 80$ and (b) 140.

where $E(t)$ is a forcing term and $\epsilon(\dot{u} - 1/3\dot{u}^3)$ is a damping term. Due to the nonlinear damping term, the oscillator is self-excited and self-limited. ω_0^* is the natural angular velocity. When $E(t) = 0$, the system oscillates with the limit-cycle frequency (Nayfeh & Mook 1979). If the magnitude of the forcing term (ϵk) is small and the difference ($\epsilon\sigma = \omega_f - \omega_0^*$) between the forcing angular velocity (ω_f) and the natural angular velocity (ω_0^*) is small, $E(t)$ can be expressed as

$$E(t) = \epsilon k \cos \omega_f t. \tag{3.2}$$

For lock-on, the response should be expressed as $u = a \cos(\omega_f t - \gamma)$, where a is the magnitude of response and γ is the phase difference. In order to obtain a lock-on solution, the frequency response equation satisfies the following relation (Nayfeh & Mook 1979):

$$\rho(1 - \rho)^2 + 4\sigma^2\rho = \frac{1}{4}k^2, \tag{3.3}$$

where $\rho = \frac{1}{4}\omega_0^{*2}a^2$. Depending on the values of ρ and σ , the response can be categorized into ‘lock-on’ and ‘non-lock-on’. In the case of $\rho > 1/2$ and $(1 - 4\rho + 3\rho^2)/4 + \sigma^2 > 0$, the system is stable, i.e. lock-on occurs. Otherwise, the response is unstable and aperiodic. For example, when $\epsilon = 0.1$, $\omega_0^* = 1.0$ and $k^2 = 2.0$, if $|\omega_f - \omega_0^*| < 0.0426$, the system is stable. However, if $|\omega_f - \omega_0^*| > 0.0426$, the system is unstable (Nayfeh & Mook 1979).

The foregoing results can be reconfirmed by solving the Van der Pol equation with the fourth-order Runge–Kutta method. The Fourier transforms are shown in figure 5. The periodic lock-on state occurs in the case of $\omega_f = 0.96$ and $\omega_f = 1.04$, as shown in figure 5(b). The no-forcing case at $\omega_0^* = 1.00$ is also shown in figure 5(b). Outside the

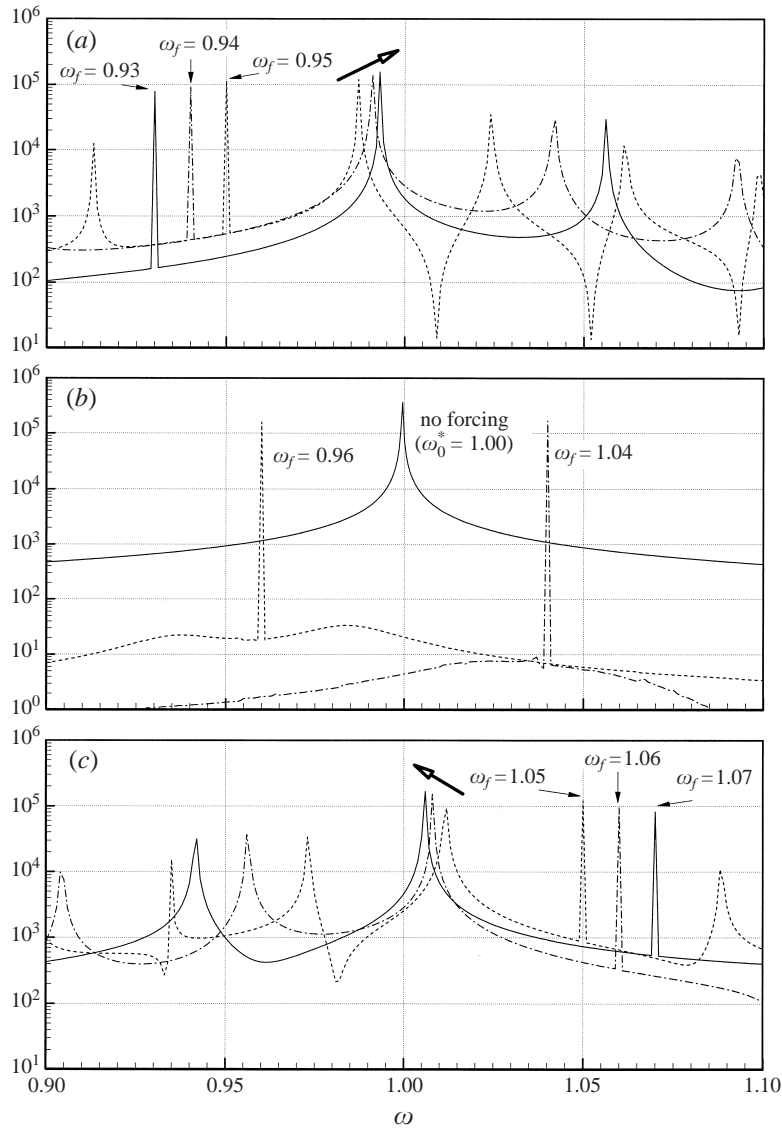


FIGURE 5. Power spectra on the Van der Pol equation: (a) below the lock-on region, (b) lock-on and (c) above the lock-on region.

lock-on range, i.e. in the cases below ($\omega_f = 0.93, 0.94$ and 0.95) and above ($\omega_f = 1.05, 1.06$ and 1.07), the responses are very similar to those of the afore-stated observations in figure 3. In particular, the converging phenomena to $\omega_0^* = 1.0$ are clearly captured in figures 5(a) and 5(c). The modulated frequencies due to nonlinear coupling on the opposite side are also observed as seen in figure 3.

Another model, the circle map, is applied to predict certain features of the wake subjected to controlled forcings (Olinger & Sreenivasan 1988; Strogatz 1994; Olinger 1998). The circle map is a universal model describing a system with two coupled oscillations. While the temporal variations are dealt with in the Van der Pol model, the phase is directly employed in the circle map.

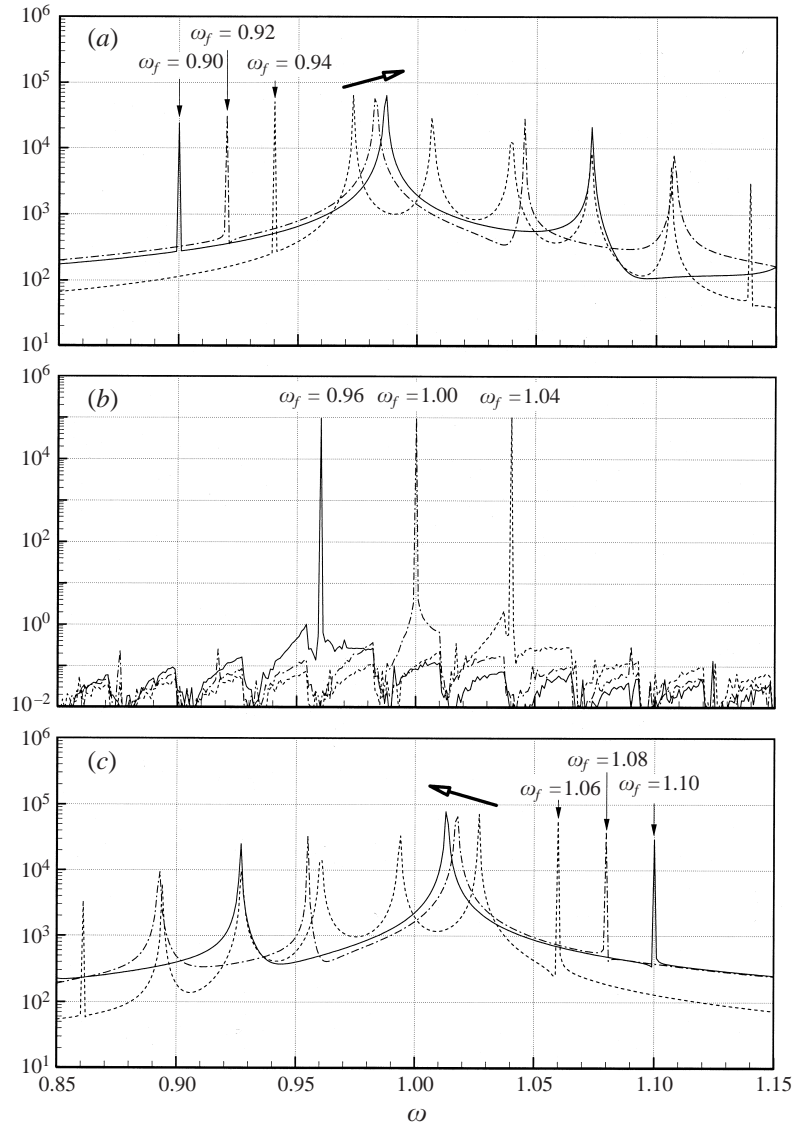


FIGURE 6. Power spectra on the circle map: (a) below the lock-on region, (b) lock-on and (c) above the lock-on region.

If the angular velocity of forcing is $\omega_f (= \Theta' = d\Theta/dt)$ and the phase of the response is ϕ , the circle map is written as

$$\omega_0 = \omega_0^* + A \sin(\Theta - \phi), \quad (3.4)$$

where ω_0 is the angular velocity of the system ($\omega_0 = d\phi/dt$), ω_0^* is the natural angular velocity and A is a resetting strength ($A > 0$) which measures the ability of the system to modify its instantaneous angular velocity. When $\omega_f > \omega_0^*$, Θ is ahead of ϕ and this yields $\sin(\Theta - \phi) > 0$ and the angular velocity of the system (ω_0) increases and converges to ω_f . On the other hand, if $\omega_f < \omega_0^*$, $\sin(\Theta - \phi) < 0$ and the opposite is true. Accordingly, lock-on occurs in the range of entrainment ($\omega_0^* - A \leq \omega_f \leq \omega_0^* + A$). The phase difference is $\Theta - \phi = \pi/2$ at $\omega_0 = \omega_f = \omega_0^* + A$

and it is shifted to $\Theta - \phi = -\pi/2$ at $\omega_0 = \omega_f = \omega_0^* - A$, which results in a response phase shift of π . As an example, equation (3.4) is solved in the range $0.80 \leq \omega_f \leq 1.20$ for $\omega_0^* = 1.00$ and $A = 0.05$ and the Fourier transform results are displayed in figure 6. The lock-on takes place at $\omega_f = 0.96, 1.00$ and 1.04 . Outside the lock-on range, the response behaviours are consistent with those in the Van der Pol equation model. These confirm the present observations, i.e. the frequency selection and the asymptotic convergence of the dominant shedding frequency (St_0) to the natural shedding frequency (St_0^*).

Based on the preceding results, a model equation is proposed to describe the frequency selection subjected to controlled forcings. The asymptotic convergence of St_0 to S_f can be modelled as

$$dSt_0/dt = -k_f(St_0 - S_f), \tag{3.5}$$

where k_f is a model function ($k_f > 0$). When $St_0 > S_f$, dSt_0/dt becomes negative and St_0 decreases. On the other hand, when $St_0 < S_f$, dSt_0/dt becomes positive and St_0 increases. Regardless of the initial value of St_0 , St_0 converges to S_f . Similarly, the convergence of St_0 to St_0^* can be written as

$$dSt_0/dt = -k_0^*(St_0 - St_0^*), \tag{3.6}$$

where k_0^* is also a model function ($k_0^* > 0$). Combining these two equations results in

$$dSt_0/dt = -k_f(St_0 - S_f) - k_0^*(St_0 - St_0^*). \tag{3.7}$$

In equation (3.7), k_f and k_0^* are weighting factors that depend on S_f , St_0^* and St_0 :

$$k_f = C_1 \exp(-C_3|S_f - St_0|) \exp(-C_4|S_f - St_0^*|), \tag{3.8}$$

$$k_0^* = C_2(1 - \exp(-C_5|S_f - St_0|)). \tag{3.9}$$

In equation (3.8), k_f represents the degree of convergence of St_0 to S_f , i.e. the extent of lock-on. The first term, $\exp(-C_3|St_0 - S_f|)$, indicates that St_0 does not converge to S_f if $|S_f - St_0|$ is very large. The second term, $\exp(-C_4|S_f - St_0^*|)$, indicates that lock-on takes place in the vicinity of St_0^* . The model function k_0^* in equation (3.9) represents the degree of convergence of St_0 to St_0^* , where the term $1 - \exp(-C_5|S_f - St_0|)$ weakens the tendency of St_0 towards St_0^* as St_0 approaches S_f . In equation (3.7), if St_0 is equal to S_f , $dSt_0/dt = 0$, then S_f is a solution. In the vicinity of St_0^* , S_f is a stable solution of equation (3.7). However, as $|S_f - St_0^*|$ exceeds a certain value, S_f becomes an unstable solution. An additional stable solution is obtained, i.e. $St_0 \approx St_0^*$. Note that the exponential function in equations (3.8) and (3.9) is employed to represent a decaying function.

Figure 7 shows a model prediction of the frequency selection obtained by solving equation (3.7). In figure 7, the solid line represents stable solutions (St_0) and the dotted line indicates unstable ones. The points designated \bullet are obtained by solving the Navier–Stokes equations in the forced wakes (figure 3). The constants in equation (3.8) and (3.9) are: $C_1 = 0.039$, $C_2 = 1.0$, $C_3 = 110$, $C_4 = 5.0$ and $C_5 = 5.4$. A comparison of the frequency selections in figure 7 discloses that the shedding frequency (St_0) changes continuously to St_0^* in the non-lock-on region after the frequency bifurcation at the lock-on boundary. The agreement between the model prediction and the numerically simulated wake results is satisfactory.

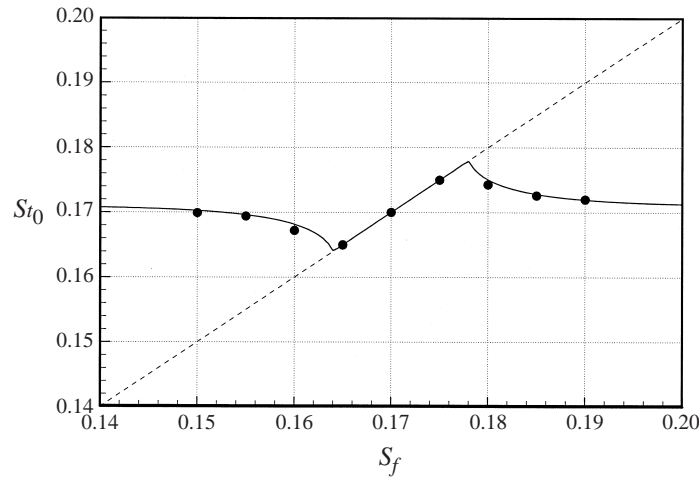


FIGURE 7. Frequency selection diagram. See text for details.

4. Analysis of quasi-periodicity

As discussed in §3, the cylinder wakes studied here show a quasi-periodic state containing two fundamental frequencies St_0 and S_f . In such a state, the lift coefficient (C_L) can be represented as a double Fourier series of the form (Ott 1996)

$$C_L(t) = \sum_{j=-\infty}^{\infty} \sum_{k=-\infty}^{\infty} a_{j,k} \cos [2\pi(jSt_0 + kS_f)t - \phi_{j,k}], \quad (4.1)$$

where $a_{j,k}$ is the amplitude and $\phi_{j,k}$ is the phase of frequency $jSt_0 + kS_f$. For all $jSt_0 + kS_f < 0$, the amplitudes $a_{j,k}$ are set to zero, i.e. $a_{j,k} = 0$. The time-averaged value of $C_L(t)$, i.e. $a_{0,0} \cos(\phi_{0,0})$ is zero for $j = k = 0$. For $j = 0$ and $k = 1$, the component of S_f is $a_{0,1} \cos(2\pi S_f t - \phi_{0,1})$. Since the forcing frequency and its superharmonics coexist in the lock-on state, equation (4.1) can be written as $C_L(t) = \sum_{k=0}^{\infty} a_{0,k} \cos(2\pi k S_f t - \phi_{0,k})$. To show the behaviour of $C_L(t)$ effectively with the forcing phase information ($\theta = 2\pi S_f t$), a diagram of $C_L(t)$ is employed by dividing $C_L(t)$ into two components, i.e.

$$a(t) = C_L(t) \cos \theta, \quad (4.2)$$

$$b(t) = C_L(t) \sin \theta. \quad (4.3)$$

This indicates that the distance from the origin ($a = 0, b = 0$) to each point is $C_L(t)$ and the angle with the a -axis is θ , i.e. $b(t)/a(t) = \tan \theta$. From such a diagram, the desired information for $C_L(\theta)$ can be acquired directly at each forcing phase θ .

For lock-on, i.e. $S_f = 0.165, 0.170$ and 0.175 , three circle diagrams are shown in figure 8. Since $a_{0,0} = 0$ and $a_{0,1} \gg a_{0,2}, a_{0,3}, \dots$, $C_L(t)$ can be written as

$$C_L(t) = C_{L_{\max}} \cos(\theta - \phi_f). \quad (4.4)$$

To obtain the above relation, it is assumed that $\phi_f \approx \phi_{0,1}$, $C_{L_{\max}} \approx a_{0,1}$ and therefore $C_L(\theta + \pi) = -C_L(\theta)$. C_L has a positive maximum ($+$) $C_{L_{\max}}$ at $\theta = \phi_f$ and a negative maximum ($-$) $C_{L_{\max}}$ at $\theta = \phi_f + \pi$. Accordingly, these two maximum points of $C_L(t)$ collapse in figure 8. The substitution of equation (4.4) into equations (4.2) and (4.3)

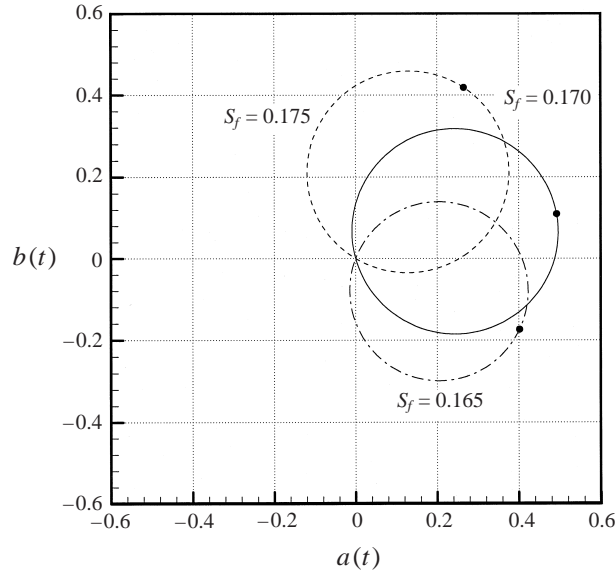


FIGURE 8. Diagrams of $C_L(t)$ at lock-on: $S_f = 0.165$, $S_f = 0.170$ and $S_f = 0.175$.

yields

$$a(t) = C_{L_{max}} \cos(\theta - \phi_f) \cos \theta = 1/2 C_{L_{max}} \cos(2\theta - \phi_f) + 1/2 C_{L_{max}} \cos \phi_f, \quad (4.5)$$

$$b(t) = C_{L_{max}} \cos(\theta - \phi_f) \sin \theta = 1/2 C_{L_{max}} \sin(2\theta - \phi_f) + 1/2 C_{L_{max}} \sin \phi_f. \quad (4.6)$$

Based on these relations, a circle equation is derived as

$$(a(t) - \frac{1}{2} C_{L_{max}} \cos \phi_f)^2 + (b(t) - \frac{1}{2} C_{L_{max}} \sin \phi_f)^2 = (\frac{1}{2} C_{L_{max}})^2. \quad (4.7)$$

In the above circle equation, the distance from the origin ($a = 0$, $b = 0$) to the centre of circle ($\frac{1}{2} C_{L_{max}} \cos \phi_f$, $\frac{1}{2} C_{L_{max}} \sin \phi_f$) is $\frac{1}{2} C_{L_{max}}$. The angle with the a -axis is ϕ_f , which is designated by black dots in figure 8. It should be noted that one forcing cycle is achieved every two revolutions.

A closer comparison of three circles for $S_f = 0.165$, 0.170 and 0.175 reveals that small changes of S_f produce large changes of ϕ_f . Once one vortex is created, a low-pressure region emerges to balance its centrifugal force. This means that the change of ϕ_f induces a switch in the phase of the initially formed vortex. For $S_f = 0.165$, the vortex is formed on the upper cylinder side in the clockwise rotation. However, for $S_f = 0.175$, it is formed in the counter-clockwise rotation. The phase change between the shedding vortex and the cylinder rotation velocity is the order of π in the lock-on region (Ongoren & Rockwell 1988; Filler *et al.* 1991; Baek & Sung 1998).

Before looking into the $C_L(t)$ variations outside the lock-on state, it is meaningful to see the flow patterns with respect to the rotational oscillation in the non-lock-on state. To observe the vortex formation modes, instantaneous streamlines from the simulations of the consecutive rotational oscillations are displayed in figures 9 and 10 for $S_f = 0.155$ and $S_f = 0.190$, respectively. The streamline snapshots are shown taken from the instant when the counter-clockwise rotation starts, i.e. the forcing phase θ is zero ($\theta = 2n\pi$). In each snapshot, the succession of streamlines corresponds to successive cycles of the rotational oscillation. The history of $C_L(t)$ is also plotted

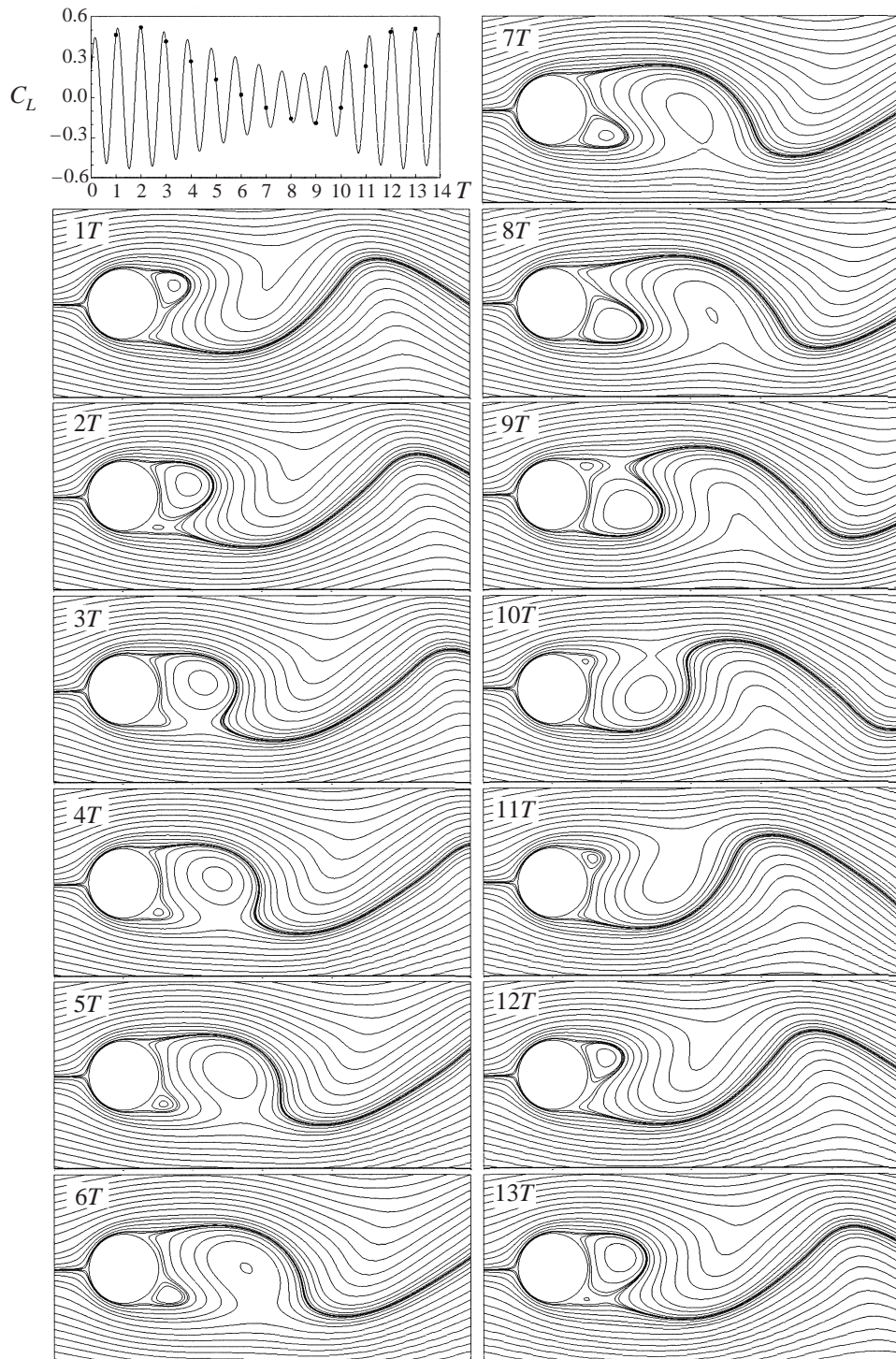


FIGURE 9. Instantaneous streamline patterns of the consecutive rotational oscillations at $S_f = 0.155$. The points in the $C_L(t)$ diagram correspond to the respective instants in the streamline pictures ($\theta = 2\pi S_f t = 2n\pi$).

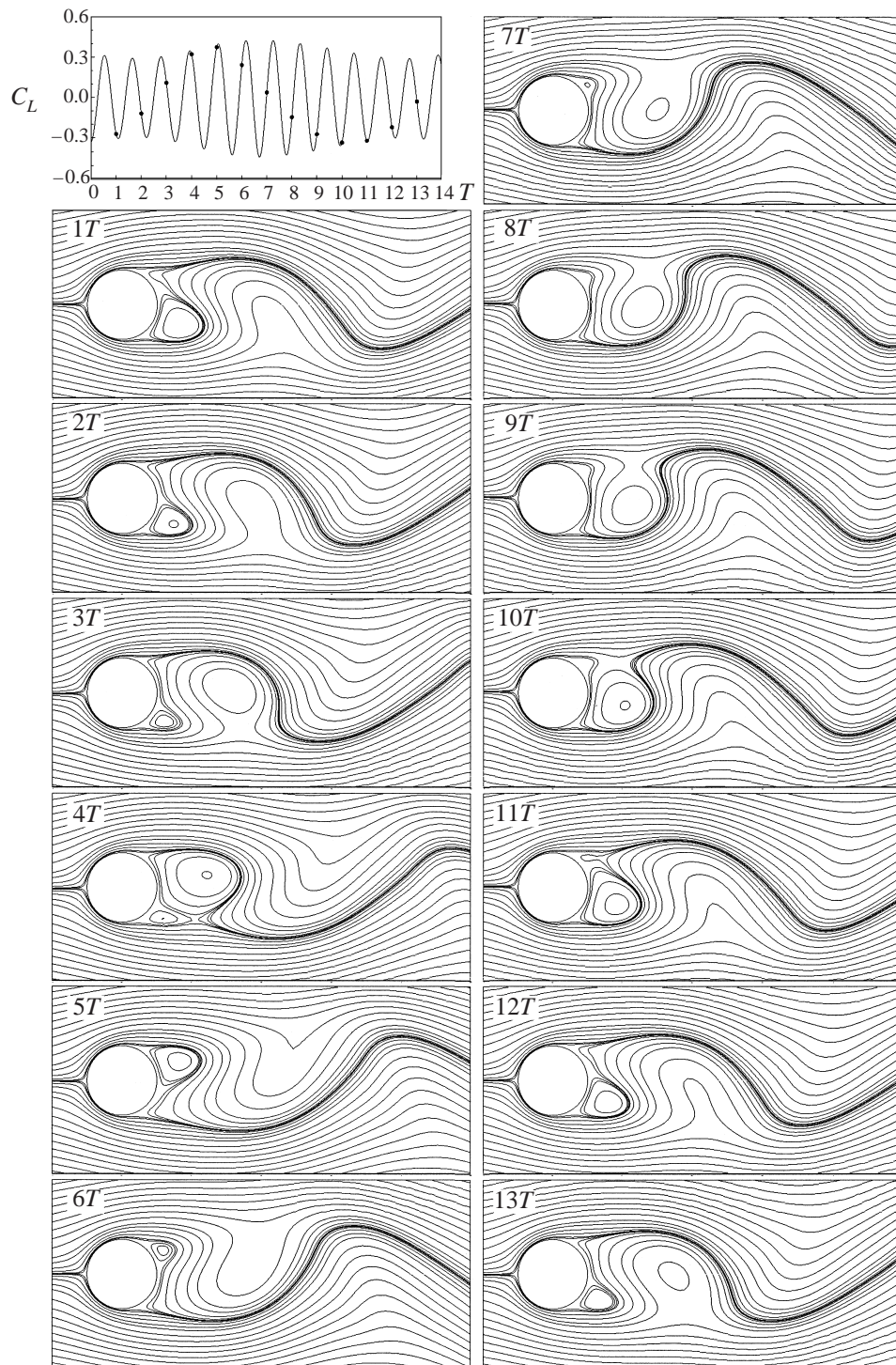


FIGURE 10. As figure 9 but at $S_f = 0.190$.

on the upper-left plot of the figure. The designated points in $C_L(t)$ correspond to the respective instants in the streamline pictures.

In the case of $S_f = 0.155$ (figure 9) where the forcing frequency is below the lower limit of lock-on, the shedding frequency ($St_0 \approx 0.169$) is slightly lower than the natural shedding frequency ($St_0^* = 0.171$). Since St_0 is higher than the forcing frequency ($S_f = 0.155$), the shedding period is shorter than the forcing period. This leads to a slight phase delay, which is also exhibited in the $C_L(t)$ history. When the flow state is examined at each forcing cycle, one cycle of the vortex shedding is completed and the next cycle has partially elapsed. During the 11 forcing periods, approximately 12 vortex sheddings occur from each side ($St_0/S_f \approx 0.169/0.155 \approx 12/11$). In figure 9, the streamline pattern at $12T$ after the 11th forcing looks similar to the original pattern at $1T$; however, it is not exactly the same. Since the ratio St_0/S_f is not rational, the flow state is quasi-periodic and the same state is never exactly recovered.

The case of $S_f = 0.190$, which is above the upper limit of lock-on, is shown in figure 10. The instantaneous streamline patterns are analogous to those presented in figure 9. The shedding frequency ($St_0 \approx 0.172$), which is slightly higher than the natural shedding frequency ($St_0^* = 0.171$), is lower than the forcing frequency ($S_f = 0.190$). Since one cycle of the vortex shedding is not completed during one forcing cycle, some additional time is required. It is observed in the $C_L(t)$ history that the phase is slightly preceded per cycle and these accumulate. After the 11 forcing periods, the streamline pattern at $12T$ in figure 10 is similar to the streamline pattern at $1T$. However, these are not exactly the same. During the 11 forcing periods, approximately 10 vortex sheddings occur ($St_0/S_f \approx 0.172/0.190 \approx 10/11$).

The afore-stated instantaneous streamline patterns are analogous to the experimental aperiodic responses of Lofty & Rockwell (1993). For example, figure 9 corresponds to figure 2(a) in Lofty & Rockwell (1993). The forcing condition is similar, e.g. the value of $S_f/St_0^* = 0.155/0.171 \approx 0.906$ is similar to that of $f_e/f_0^* = 0.87$ in Lofty & Rockwell (1993). The upper vortex moves away from the cylinder with increasing number of forcing cycles. For excitation at frequencies above the upper limit of lock-on, figure 10 ($S_f/St_0^* = 0.190/0.171 \approx 1.11$) is similar to figure 2(b) in Lofty & Rockwell (1993) ($f_e/f_0^* = 1.25$). The upper vortex moves towards the cylinder with each successive forcing cycle.

The $C_L(t)$ diagrams for non-lock-on are displayed in figure 11, where the axes $a(t)$ and $b(t)$ are defined in equations (4.2) and (4.3). The solid line represents the averaged value of $C_L(t)$ at each forcing phase ($\theta = 2\pi S_f t$), which is denoted by $C_{L_{ave}}(\theta)$. The dash-dot line represents the positive and negative maximum values of $C_L(t)$ at θ , i.e. $C_{L_{max+}}(\theta)$ and $C_{L_{max-}}(\theta)$. The dotted line represents the differences between $C_{L_{ave}}(\theta)$ and $C_{L_{max\pm}}(\theta)$, which are defined as

$$C_{L_{diff+}}(\theta) = C_{L_{max+}}(\theta) - C_{L_{ave}}(\theta), \quad (4.8)$$

$$C_{L_{diff-}}(\theta) = C_{L_{max-}}(\theta) - C_{L_{ave}}(\theta). \quad (4.9)$$

With these definitions, the behaviour of $C_L(t)$ versus θ can be analysed with respect to S_f . For example, in the case of $S_f = 0.160$, the following can be obtained from figure 11(c): $C_{L_{ave}}(0.50\pi) = (-)0.103$ at $\theta = 0.50\pi$ and $C_{L_{ave}}(1.50\pi) = (+)0.103$ at $\theta = 1.50\pi (= -0.50\pi)$, i.e. $C_{L_{ave}}(\theta + \pi) = -C_{L_{ave}}(\theta)$. The marked point on the solid line indicates that the maximum $C_{L_{ave}}(\theta)$ is at $\theta = 1.80\pi (= -0.20\pi)$. Recall that the rotational oscillation is defined as $\Omega = \Omega_{max} \sin(2\pi S_f t)$. This suggests that the positive maximum of $C_{L_{ave}}(\theta)$ is obtained when the clockwise velocity is reduced. It is known from the definition of $C_{L_{max\pm}}(\theta)$ that all instantaneous points of $a(t)$ and

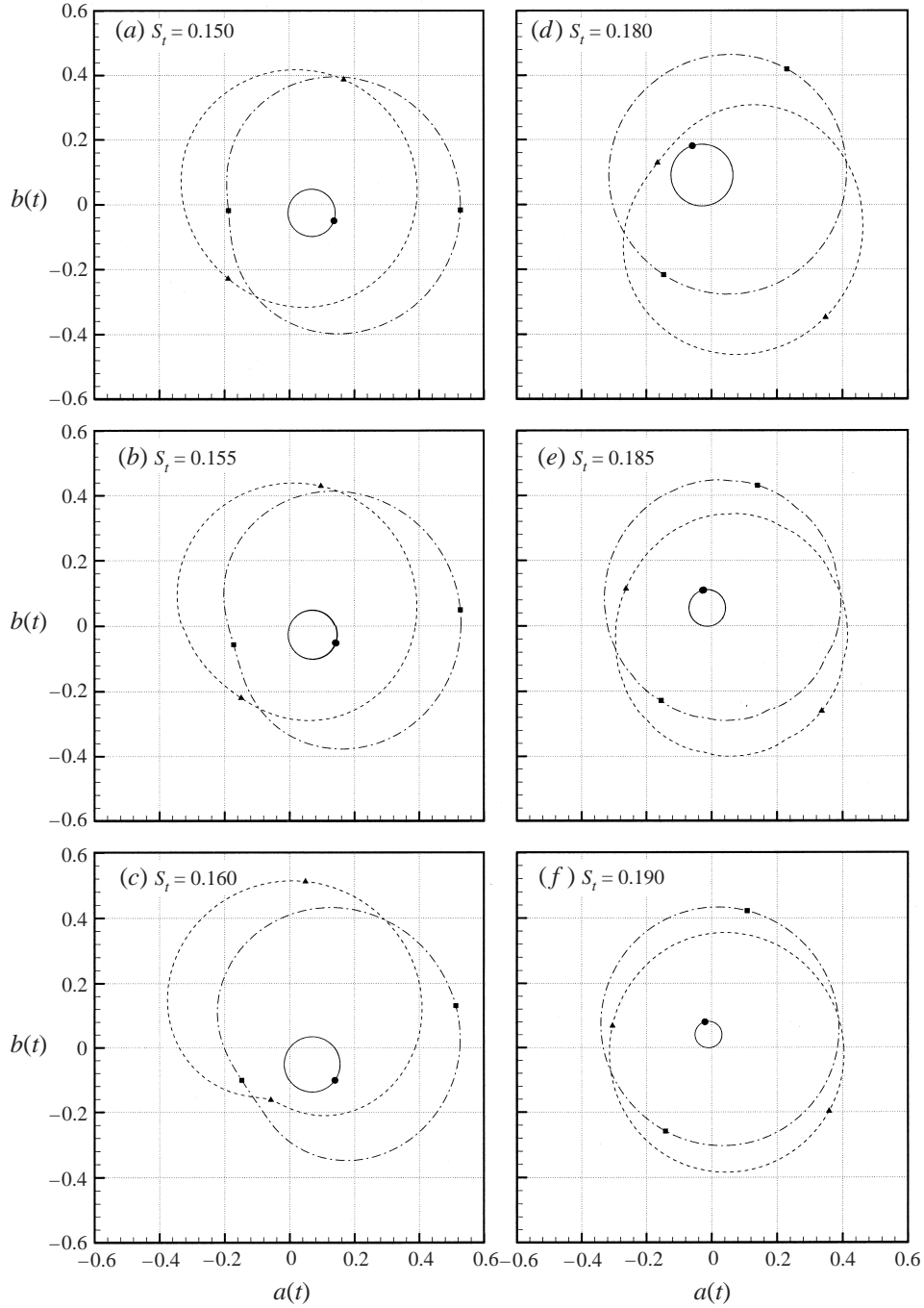


FIGURE 11. Diagrams of $C_{L_{ave}}(\theta)$, $C_{L_{max\pm}}(\theta)$ and $C_{L_{diff\pm}}(\theta)$ at non-lock-on: $C_{L_{ave}}$ (solid), $C_{L_{max\pm}}$ (dash-dot) and $C_{L_{diff\pm}}$ (dashed).

$b(t)$ are within the dash-dot line. Since the closed diagram of $C_{L_{max+}}(\theta)$ is the same as that of $C_{L_{max-}}(\theta)$, $C_{L_{max+}}(\theta)$ is equal to $-C_{L_{max-}}(\theta + \pi)$, e.g. $C_{L_{max+}}(0.50\pi) = (+)0.411$ and $C_{L_{max-}}(0.50\pi) = (-)0.291$. In the opposite phase, $C_{L_{max+}}(1.50\pi) = (+)0.291$ and $C_{L_{max-}}(1.50\pi) = (-)0.411$. From the definitions of equations (4.8) and (4.9), $C_{L_{diff+}}(\theta)$

is equal to $-C_{L_{diff-}}(\theta + \pi)$. It is shown in figure 11 that they collapse exactly. For example, when $S_f = 0.160$, $C_{L_{diff+}}(0.50\pi) = (+)0.514$ and $C_{L_{diff-}}(0.50\pi) = (-)0.188$. In the opposite phase, $C_{L_{diff+}}(1.50\pi) = (+)0.188$ and $C_{L_{diff-}}(1.50\pi) = (-)0.514$. However, it should be noted that $C_{L_{ave}}(\theta)$ is not the same as the mean value of $C_{L_{max+}}(\theta)$ and $C_{L_{max-}}(\theta)$.

An examination of figure 11 indicates that the size of $C_{L_{ave}}(\theta)$ is reduced as S_f moves away from the lock-on boundary. This means that the magnitude of the S_f component decreases as $|S_f - St_0^*|$ increases. Another finding concerning $C_{L_{ave}}(\theta)$ is that the maximum phases of $C_{L_{ave}}(\theta)$ at lower forcing frequencies are located on the opposite side to those at higher forcing frequencies. The phase differences in the lock-on region are preserved in the non-lock-on region.

In contrast to the changes of $C_{L_{ave}}(\theta)$ just noted, the size change of $C_{L_{max+}}(\theta)$ is not substantial. This may be attributed to the fact that the instantaneous maximum values of $C_L(t)$ do not vary significantly in the forcing cases. It is seen in figure 11 that the phase of the maximum $C_{L_{max+}}(\theta)$ is not the same as that of $C_{L_{ave}}(\theta)$. The phase difference between them is small for $S_f = 0.150$ and $S_f = 0.190$, while it is significant for $S_f = 0.160$ and $S_f = 0.180$. These differences are dependent on the distribution of $C_{L_{diff\pm}}(\theta)$. If the diagram of $C_{L_{diff\pm}}(\theta)$ has a circle shape, $C_{L_{diff\pm}}(\theta)$ is constant and independent of θ . When S_f is far away from the lock-on boundary, it is seen that the shape of $C_{L_{diff\pm}}(\theta)$ is closer to a circle shape and the corresponding phase difference decreases. These phenomena can be explained by the presence of modulated frequencies, which will be seen later.

Specification of one phase can be regarded geometrically as specifying a point on a circle. Specification of two phases can be regarded geometrically as specifying a point on a two-dimensional toroidal surface. Provided that the two phases are incommensurate, the orbit on the torus never closes on itself. As time goes to infinity, the orbit will eventually come close to every point on the toroidal surface (Ott 1996). By utilizing the torus concept, the afore-stated quasi-periodicity can be described effectively. Since the curved surface of a torus makes it hard to draw phase trajectories, an equivalent representation is employed: a square with periodic boundary condition. Then, if a trajectory runs off a boundary, it reappears on the opposite boundary. The forcing phase is defined as $\theta = 2\pi S_f t + \theta_0$ and the shedding phase as $\varphi = 2\pi S t_0 t + \varphi_0$. Trajectories with the coordinates θ and φ are shown in figure 12(a,b), where the corresponding trajectories are straight lines with constant slope $St_0/S_f = p/q$. Two examples at $\theta_0 = 0$ and $\varphi_0 = 0$ are shown in figure 12: (a) $St_0/S_f = p/q = 4/3$ and (b) $St_0/S_f = p/q = 17/15$.

There are two qualitatively different cases, depending on whether the slope p/q is a rational or an irrational number. If the slope is rational, all trajectories are closed, because θ completes q revolutions in the same time that φ completes p revolutions. The initial positions are determined by θ_0 and φ_0 . If the slope is irrational, then the flow is said to be quasi-periodic. Every trajectory is continued endlessly on the square, never intersecting itself and yet never quite closing. Each trajectory is dense on the square: in other words, each trajectory comes arbitrarily close to any given point on the square. This is not to say that the trajectory passes through each point; it just comes arbitrarily close. Therefore, the initial values θ_0 and φ_0 are meaningless. By adding the modulation phase, it can be extended to a three-dimensional regular hexahedron. The modulation phase φ_m is defined as $\varphi_m = 2\pi S_m t + \varphi_{m_0}$, where S_m is the first modulated frequency $S_m = S_{m_{2-1}} = 2St_0 - S_f$. After some substitution φ_m can be rewritten as $\varphi_m = 2\varphi - \theta + \varphi_{m_0}$, where φ_{m_0} is the modulation phase at the instant $t = 0$. The instant $t = 0$ is set when $\theta = 2n_1\pi$ and $\varphi = 2n_2\pi$, where n_1 and n_2 are

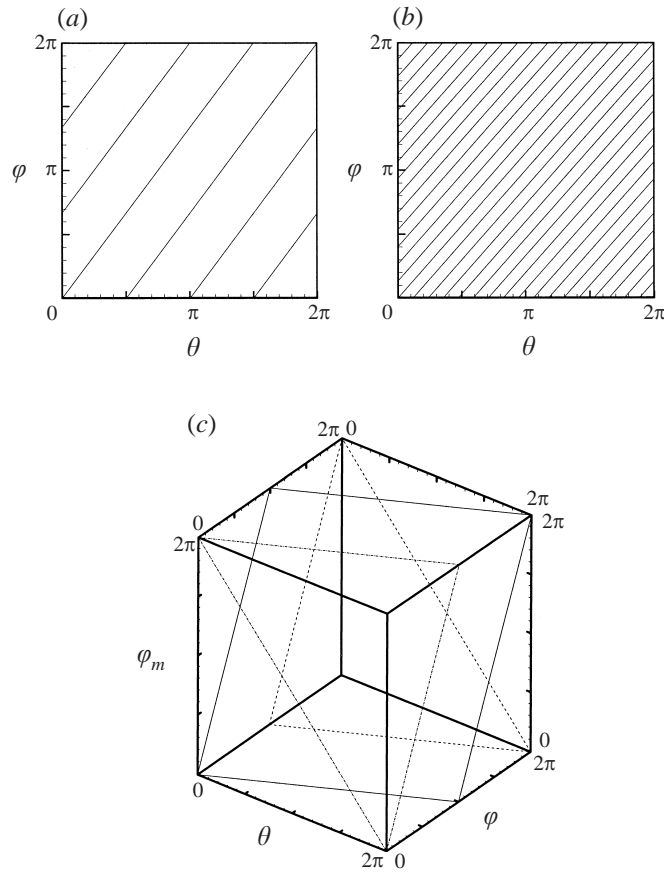


FIGURE 12. Two-frequency quasi-periodic trajectories on a square and a hexahedron: (a) $St_0/S_f = 4/3$, (b) $St_0/S_f = 17/15$ and (c) St_0/S_f is irrational.

integers. A three-dimensional trajectory $(\theta, \varphi, \varphi_m)$ is plotted in figure 12(c), where the initial phase is $\varphi_{m_0} = 0$. As shown, it constitutes several planes with respect to the lines of infinite length. The positions are determined by φ_{m_0} .

The lift coefficient $C_L(t)$ in equation (4.1) can be written in terms of three dominant frequencies

$$C_L(t) \approx A_f \cos(2\pi S_f t - \phi_f) + A_0 \cos(2\pi S t_0 t - \phi_0) + A_m \cos(2\pi S_m t + \varphi_{m_0} - \phi_m), \tag{4.10}$$

where A_f , A_0 and A_m denote the magnitudes of three frequency components S_f , $S t_0$ and S_m . Taking a phase average at every $\theta (= 2\pi S_f t)$ results in the second and third terms in equation (4.10) going to zero. This is due to the fact that St_0/S_f is irrational. Accordingly, the phase-averaged value of $C_L(t)$ is $C_{L_{ave}}(\theta) = A_f \cos(\theta - \phi_f)$. $C_{L_{ave}}(\theta)$ is represented by the solid line in figure 13. Note that this is the same as the solid line in figure 11.

By using the modulation relation $S_m = 2S t_0 - S_f$, equation (4.10) can be rewritten as

$$C_L(\theta, \varphi) = A_f \cos(\theta - \phi_f) + A_0 \cos(\varphi - \phi_0) + A_m \cos(2\varphi - \theta + \varphi_{m_0} - \phi_m). \tag{4.11}$$

If the modulated frequency term is not considered ($A_m = 0$), $C_L(\theta, \varphi)$ has the maximum

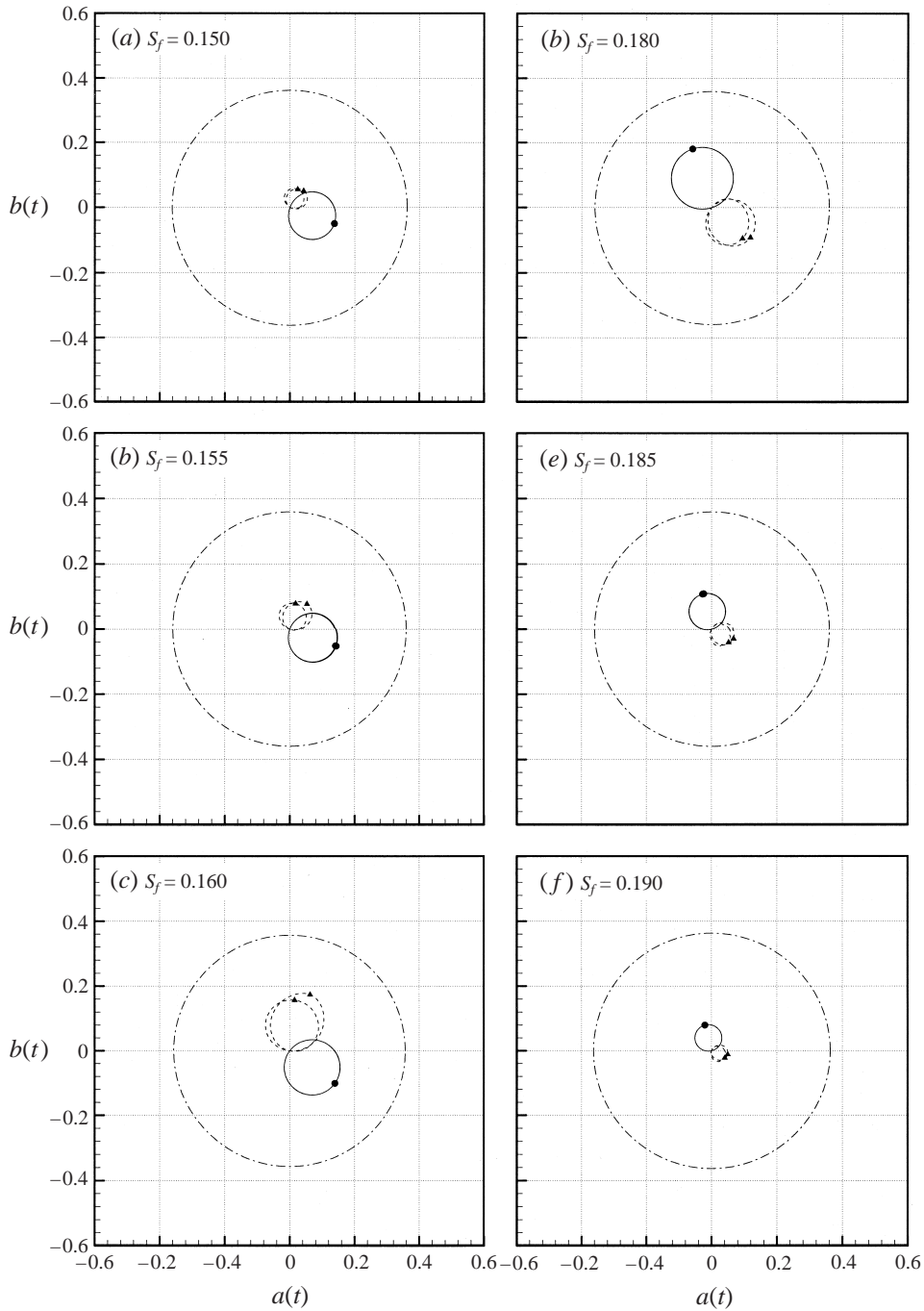


FIGURE 13. Frequency component diagrams of $C_L(\theta)$ at non-lock-on: S_f (solid), St_0 (dash-dot) and S_m (dashed).

value $A_f + A_0$ when the point (θ, φ) comes arbitrarily close to the point (ϕ_f, ϕ_0) . This gives $C_{L_{max+}}(\theta) = A_f \cos(\theta - \phi_f) + A_0$ and $C_{L_{diff+}}(\theta) = A_0$. The maximum phase of $C_{L_{max+}}(\theta)$ is then equal to that of $C_{L_{ave}}(\theta)$, i.e. ϕ_f . However, due to the presence of the modulated frequency term (S_m) in reality, the above relation is not valid. Since

$A_0 > A_f > A_m$, when $C_L(\theta, \varphi)$ has maximum, the shedding phase φ is approximated as $\varphi \approx \phi_0$ and equation (4.11) reduces to

$$C_{L_{\max+}}(\theta) = A_f \cos(\theta - \phi_f) + A_0 + A_m \cos(2\phi_0 - \theta + \varphi_{m_0} - \phi_m). \quad (4.12)$$

Note that the modulated frequency term is a function of θ . If $\varphi_{m_0} = \phi_f + \phi_m - 2\phi_0$, the phase of the maximum $C_{L_{\max+}}(\theta)$ is ϕ_f , which is the same as that of $C_{L_{\text{ave}}}(\theta)$. The value of $C_{L_{\max+}}(\phi_f)$ is then $C_{L_{\max+}}(\phi_f) = A_f + A_0 + A_m$ upon substitution of ϕ_f into equation (4.12). For arbitrary φ_{m_0} , it shows that the maximum value of $C_{L_{\max+}}(\theta)$ is $A_0 + [A_f^2 + A_m^2 + 2A_f A_m \cos(\varphi_{m_0} + 2\phi_0 - \phi_f - \phi_m)]^{1/2}$. The phase of the maximum $C_{L_{\max+}}(\theta)$ is not ϕ_f only, but it is also dependent on A_f , A_m , φ_{m_0} , and ϕ_m as well.

Figure 13 shows the frequency component diagrams of $C_{L_{\max+}}(\theta)$. The solid, dash-dot and dashed lines represent the first (forcing), the second (shedding) and the third (modulated) terms of $C_{L_{\max+}}(\theta)$ in equation (4.12), respectively. The maximum values are marked on the diagrams. Note that the solid line is the same as that of $C_{L_{\text{ave}}}(\theta)$ in figure 11. Corresponding to equation (4.12), $C_{L_{\text{diff+}}}(\theta)$ in equation (4.8) can be rearranged as

$$C_{L_{\text{diff+}}}(\theta) = A_0 + A_m \cos(2\phi_0 - \theta + \varphi_{m_0} - \phi_m) = \bar{C}_{L_{\text{diff+}}} + C'_{L_{\text{diff+}}}(\theta), \quad (4.13)$$

where $\bar{C}_{L_{\text{diff+}}}$ is the averaged value of $C_{L_{\text{diff+}}}(\theta)$ and is equivalent to A_0 in equation (4.12). $C'_{L_{\text{diff+}}}(\theta)$ corresponds to the third term in equation (4.12), i.e. $C'_{L_{\text{diff+}}}(\theta) = A_m \cos(2\phi_0 - \theta + \varphi_{m_0} - \phi_m)$. This yields $C_{L_{\max+}}(\theta) = C_{L_{\text{ave}}}(\theta) + \bar{C}_{L_{\text{diff+}}} + C'_{L_{\text{diff+}}}(\theta)$.

As shown in figure 13, the size of the solid circles decreases as S_f moves away from the lock-on boundary. This suggests that the direct response of S_f to C_L weakens outside the lock-on range. The changes of the dash-dot circles are small, which means that the strength of a shedding vortex is not significantly affected by the forcing frequency (S_f). However, it is known that the frequency selection of St_0 depends on S_f . A closer inspection of the dotted lines in figure 13 indicates that the magnitude of $S_m (= S_{m_{2-1}} = 2St_0 - S_f)$ increases as S_f is closer to the lock-on boundary. The magnitudes of $C'_{L_{\text{diff+}}}(\theta)$ at $S_f = 0.160$ and 0.180 are then larger than those at $S_f = 0.150$ and 0.190 . Since the S_m component is a result of St_0 and S_f , the magnitude of the S_m component increases as the magnitude of the S_f component increases.

Since $S_m (= S_{m_{2-1}})$ induces the subsequent second modulated frequency $S_{m_{3-2}} = 3St_0 - 2S_f$, its magnitude increases as the magnitude of the S_m component increases. Consequently, $S_{m_{3-2}}$ also induces $S_{m_{4-3}}$. If the frequency component of $S_{m_{3-2}}$ is expressed in the form of equation (4.10), it is written as $A_{m_{3-2}} \cos(2\pi S_{m_{3-2}} t + \varphi_{m_{3-2_0}} - \phi_{m_{3-2}})$. After rearrangement similar to the prior S_m term in equation (4.11), it can be rewritten as $A_{m_{3-2}} \cos(3\varphi - 2\theta + \varphi_{m_{3-2_0}} - \phi_{m_{3-2}})$, which is a function of 2θ for $\varphi = \phi_0$. When the other modulated frequency components ($S_{m_{3-2}}$, $S_{m_{4-3}}$, ..., etc.) are included in equation (4.10), $C'_{L_{\text{diff+}}}(\theta)$ is not exactly equal to $A_m \cos(2\phi_0 - \theta + \varphi_{m_0} - \phi_m)$ in this case, however, but also includes all components of the modulated frequencies such as $S_{m_{3-2}}$. For $C'_{L_{\text{diff+}}}(\theta) = A_m \cos(2\phi_0 - \theta + \varphi_{m_0} - \phi_m)$, the shapes of the dashed diagram are circular like those in figure 8. However, since $C'_{L_{\text{diff+}}}(\theta)$ includes all modulated terms such as the 2θ term in $S_{m_{3-2}}$, the shapes are slightly non-circular. In the cases of $S_f = 0.160$ and $S_f = 0.180$, which are near the lock-on boundary, the shapes are far from circles. This is because the magnitude of the $S_{m_{3-2}}$ component is large. Near the lock-on boundary, since the magnitude of the S_f component is large, S_m and $S_{m_{j,k}}$ are also large. However, the intervals between $S_{m_{j,k}}$ are relatively small. This forms a distributed spectrum band at the lock-on boundary. The origin of the broad frequencies appears to be a competition between natural and forcing modes.

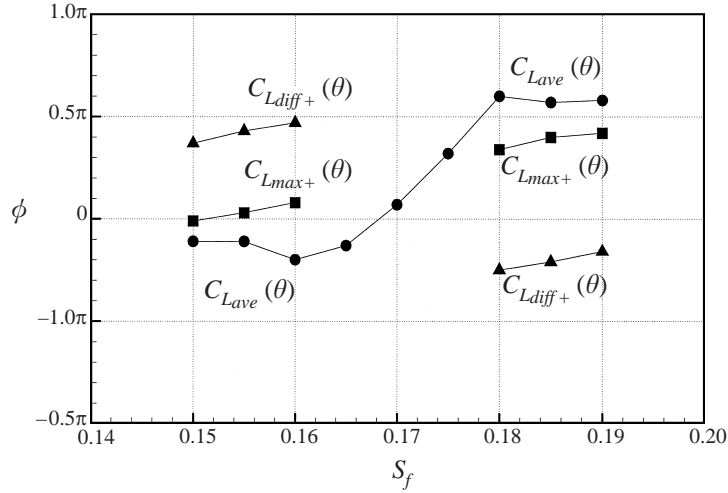


FIGURE 14. Phase distributions of maximum $C_{L_{ave}}(\theta)$, $C_{L_{max+}}(\theta)$ and $C_{L_{diff+}}(\theta)$.

The interaction of two modes gives rise to slow oscillation and chaos. The pattern competition might well be a fairly common sources of chaos (Ciliberto & Gollub 1984).

The maximum phases of $C_{L_{ave}}(\theta)$, $C_{L_{max+}}(\theta)$ and $C_{L_{diff+}}(\theta)$ are plotted against S_f in figure 14, where all the diagrams of C_L phases from figures 8 and 11 are summarized. The phase of the maximum $C_{L_{ave}}(\theta)$ is ϕ_f from equation (4.10). It is shown that the change of ϕ_f is on the order of π ($-0.20\pi \leq \phi_f \leq 0.60\pi$). This represents a phase shift of the vortex formation process of nearly π . In the circle map in figure 6, the change is exactly π . The phases of $C_{L_{max+}}(\theta)$ are not the same as those of $C_{L_{ave}}(\theta)$, as is evident in figure 14, the phase of $C_{L_{ave}}(\theta)$ is out of phase with $C_{L_{diff+}}(\theta)$. The phase of $C_{L_{max+}}(\theta)$ is located between $C_{L_{diff+}}(\theta)$ and $C_{L_{ave}}(\theta)$. Since the magnitude of $C_{L_{ave}}(\theta)$ is larger than that of $C_{L_{diff+}}(\theta)$, the phase of $C_{L_{max+}}(\theta)$ is closer to $C_{L_{ave}}(\theta)$. Accordingly, the influence of $C_{L_{ave}}(\theta)$ on $C_{L_{max+}}(\theta)$ is offset by $C_{L_{diff+}}(\theta)$. As S_f is far away from the lock-on boundary, the phase difference and the magnitude of $C_{L_{diff+}}(\theta)$ decreases. This leads to a weakened offset. However, since the magnitude of $C_{L_{ave}}(\theta)$ decreases concurrently, $C_{L_{max+}}(\theta)$ is not changed significantly.

5. Conclusions

Detailed numerical analyses have been performed to delineate the quasi-periodicity in forced wakes. A direct numerical simulation has been used to portray the unsteady dynamics of wake flows behind a circular cylinder. The Reynolds number based on the diameter is $Re = 110$ and excitation is given by the rotational oscillation of circular cylinder. The natural shedding frequency is $St_0^* = 0.171$ and the forcing frequency (S_f) varies in a range $0.150 \leq S_f \leq 0.190$. The maximum rotation velocity is 5.0% of the free-stream velocity ($\Omega_{max} = 0.05$).

The response of the forced wake can be categorized into 'lock-on' and 'non-lock-on' states. In the lock-on state, the wake structure is periodic and does not change from cycle to cycle. The shedding frequency (St_0) coincides with the forcing frequency (S_f). Outside the lock-on range, the flow structure is not phase-locked with respect to the cylinder motion because perturbations produced by both S_f and St_0 coexist

in the near wake. St_0 is not concentrated at St_0^* , but gradually converges to St_0^* . The forced frequency bifurcates into two frequencies: one follows S_f and the other (St_0) asymptotically tends to St_0^* . The additional frequency modulations are due to nonlinear coupling where the interval between the modulated frequencies is equivalent to the interval between St_0 and S_f . The magnitude comparison of frequencies shows that $St_0 > S_f > S_{mjk}$. When S_f is close to the lock-on boundary, the interval between S_f and St_0 becomes very narrow and their magnitudes are almost the same. This forms a distributed spectrum band at the lock-on boundary. As S_f approaches the boundary of lock-on, the responses are characterized by a richness in frequency content and relatively broadened spectral densities. The afore-stated frequency bifurcation and the corresponding convergence of St_0 to St_0^* can be verified by solving the Van der Pol equation and the circle map. A new frequency selection formula is proposed as functions of St_0^* and S_f . The agreement between the model prediction by the formula and the wake results is shown to be satisfactory. Instantaneous streamlines of the consecutive rotational oscillations are examined. Below the lower limit of lock-on, the shedding period is shorter than the forcing period. When the flow state is examined at each forcing cycle, one cycle of the vortex shedding is completed and the next cycle elapses partially. This leads to a slight phase delay. Above the upper limit of lock-on, the shedding period is longer than the forcing period. Since one cycle of the vortex shedding is not completed during one forcing cycle, some additional time is required. The phase is slightly preceded per cycle.

The diagrams of $C_L(t) \cos \theta$ and $C_L(t) \sin \theta$ are displayed to show the behaviour of $C_L(t)$ with the forcing phase information ($\theta = 2\pi S_f t$) in both periodic and quasi-periodic states. For lock-on, the relation $C_L(\theta + \pi) = -C_L(\theta)$ is satisfied and the diagram has a circular shape. The centre of the circle is $(\frac{1}{2}C_{L_{max}} \cos \phi_f, \frac{1}{2}C_{L_{max}} \sin \phi_f)$. The change of ϕ_f induces a switch in the phase of the initially formed vortex. The quasi-periodic states are interpreted in terms of the torus concept and the $C_L(t)$ diagram. In the quasi-periodic state, $C_L(t)$ can be written in terms of three dominant frequencies, i.e. S_f , St_0 and S_m . The sizes of S_f diagrams decrease as S_f moves away from the lock-on boundary. This suggests that the direct response of S_f to C_L weakens outside the lock-on range. The changes of St_0 diagrams are seen to be small, which means that S_f has little effect on the strength of shedding vortex. The magnitude of S_m increases as S_f approaches the lock-on boundary. Since the S_m component is made up of St_0 and S_f , the magnitude of the S_m component increases as the magnitude of the S_f component increases.

This work was supported by a grant from the National Research Laboratory of the Ministry of Science and Technology, Korea. The partial support of KORDIC supercomputer center (1998 Cray R&D Program) is also acknowledged. The authors would like to express our gratitude to Professor Haecheon Choi, who provided valuable informations on programing.

REFERENCES

- BAEK, S.-J. & SUNG, H. J. 1998 Numerical simulation of the flow behind a rotary oscillating circular cylinder. *Phys Fluids* **10**, 869.
- BEARMAN, P. W. 1984 Vortex shedding from oscillating bluff bodies. *Ann. Rev. Fluid Mech.* **16**, 195.
- BISHOP, R. E. D. & HASSAN, A. Y. 1964 The lift and drag forces on a circular cylinder oscillating in a flowing fluid. *Proc. R. Soc. Lond. A* **227**, 51.
- BLEVINS, R. D. 1985 The effect of sound on vortex shedding from cylinders. *J. Fluid Mech.* **161**, 217.
- CHOI, H., MOIN, P. & KIM, J. 1992 Turbulent drag reduction: studies of feedback control and

- flow over riblets. *Rep. TF-55*. Department of Mechanical Engineering, Stanford University, Stanford, CA.
- CHOI, H., MOIN, P. & KIM, J. 1993 Direct numerical simulation of turbulent flow over riblets. *J. Fluid Mech.* **255**, 503.
- CHYU, C. K. & ROCKWELL, D. 1996 Near-wake structure of an oscillating cylinder: effect of controlled shear-layer vortices. *J. Fluid Mech.* **322**, 21.
- CILIBERTO, S. & GOLLUB, J. P. 1984 Pattern competition leads to chaos. *Phys. Rev. Lett.* **52**, 922.
- FEY, U., KÖNIG, M. & ECKELMANN, H. 1998 A new Strouhal-Reynolds-number relationship for the circular cylinder in the range $47 < Re < 2 \times 10^5$. *Phys. Fluids* **10**, 1547.
- FILLER, J. R., MARSTON, P. L. & MIH, W. C. 1991 Response of the shear layers separating from a circular cylinder to small-amplitude rotational oscillations. *J. Fluid Mech.* **231**, 481.
- GRIFFIN, O. M. & HALL, M. S. 1991 Review-vortex Shedding lock-on and flow control in bluff body Wakes. *Trans. ASME I: J. Fluids Engng* **113**, 526.
- HARTLEN, R. T. & CURRIE, I. G. 1970 Lift-oscillator model of vortex-shedding induced vibration. *J. Engng Mech. Div. ASCE* **96**, 577.
- IWAN, W. D. & BLEVINS, R. D. 1974 A model for vortex induced oscillation of structures. *Trans. ASME E: J. Appl. Mech.* **41**, 581.
- KARNIADAKIS, G. E. & TRIANTAFYLLOU, G. S. 1989 Frequency selection and asymptotic states in laminar wakes. *J. Fluid Mech.* **199**, 441.
- KOOPMAN, G. H. 1967 The vortex wakes of vibrating cylinders at low Reynolds numbers. *J. Fluid Mech.* **28**, 501.
- LOFTY, A. & ROCKWELL, D. 1993 The near-wake of an oscillating trailing edge: mechanisms of periodic and aperiodic response. *J. Fluid Mech.* **251**, 173.
- NAYFEH, A. H. & MOOK, D. T. 1979 *Nonlinear Oscillations*. John Wiley & Sons.
- OERTEL, H. 1990 Wakes behind blunt bodies. *Ann. Rev. Fluid Mech.* **22**, 539.
- OLINGER, D. J. 1998 A low-order model for vortex shedding patterns behind vibrating flexible cable. *Phys. Fluids* **10**, 1953.
- OLINGER, D. J. & SREENIVASAN, K. R. 1988 Nonlinear dynamics of the wake of an oscillating cylinder. *Phys. Rev. Lett.* **60**, 797.
- ONGOREN, A. & ROCKWELL, D. 1988 Flow structure from an oscillating cylinder Part 1. Mechanisms of phase shift and recovery in the near wake. *J. Fluid Mech.* **191**, 197.
- OTT, E. 1993 *Chaos in Dynamical Systems*. Cambridge University Press.
- PAULEY, L. L., MOIN, P. & REYNOLDS, W. C. 1990 The structure of two dimensional separation. *J. Fluid Mech.* **220**, 397.
- SARPKAYA, T. 1979 Vortex-induced oscillations: a selective review. *Trans. ASME E: J. Appl. Mech.* **26**, 241.
- STANSBY, P. K. 1976 The locking-on of vortex shedding due to the cross-stream vibration of circular cylinders in uniform and shear flows. *J. Fluid Mech.* **74**, 641.
- STROGATZ, S. H. 1994 *Nonlinear Dynamics and Chaos*. Addison-Wesley.
- SUNG, H. J., HWANG, K. S. & HYUN, J. M. 1994a Experimental study on mass transfer from a circular cylinder in pulsating flow. *Intl J. Heat Mass Transfer* **37**, 2203.
- SUNG, H. J., KIM, Y. N. & HYUN, J. M. 1994b Discrete vortex simulation of pulsating flow behind a normal plate. *Trans. ASME I: J. Fluids Engng* **116**, 862.
- TOKUMARU, P. T. & DIMOTAKIS, P. E. 1991 Rotary oscillation control of a cylinder wake. *J. Fluid Mech.* **224**, 77.
- VAN ATTA, C. W. & GHARIB, M. 1987 Ordered and chaotic vortex streets behind circular at low Reynolds numbers. *J. Fluid Mech.* **174**, 113.
- WILLIAMSON, C. H. K. 1989 Oblique and parallel modes of vortex shedding in the wake of a circular cylinder at low Reynolds numbers. *J. Fluid Mech.* **206**, 579.
- WILLIAMSON, C. H. K. 1996 Vortex dynamics in the cylinder wake. *Ann. Rev. Fluid Mech.* **28**, 477.